EurJIC
European Journal of Inorganic Chemistry

Research Article
doi.org/10.1002/ejic.202400446

Chemistry Europe
European Chemical Societies Publishing

www.eurjic.org

The Effect of the Surrounding Matrix on Spin Transition Nanoparticles: How Shell Characteristics Alter Core Elastic Properties in Core-Shell Particles

John M. Cain,[a] Wanhong He,[a] Mark W. Meisel,*[b] and Daniel R. Talham*[a]

A surrounding matrix is known to alter nanoparticle spin transitions, the solid state structural phase changes associated with transitions between high spin (HS) and low spin(LS) states. To better quantify how the spin transition solid and surrounding matrix interact, several series of core-shell particles were prepared based on $Rb_xCo[Fe(CN)_6]_z \cdot nH_2O$, RbCoFe-PBA, as spin transition core with isostructural shells of different compositions and thicknesses. Synchrotron PXRD through the thermal high HS to LS, the LS to photoexcited high spin (PXHS), and thermal PXHS to LS transitions, show the activation energy is lowered as shells become thicker and stiffer. Calorimetry data coupled with transition state theory analysis indicate the core stiffens in the core-shell particles relative to the uncoated particles. The conclusion is supported by microstrain analysis that shows stiffer shells limit the extent to which the core distorts as individual sites transition, leading to the lower activation energy. Finally, differences in lattice mismatch with different shell materials are shown to alter the mechanism by which the transition progresses.

Introduction

Spin transition solids, including spin crossover compounds,[1,2] are often explored for applications as sensors, photonic switches, and information storage media,[1,3,4] stemming from bistability switchable with external stimuli that include temperature, light, pressure, and magnetic field, as well as by chemical changes.[5–8] Spin state changes in solid-state compounds can alter magnetism, dielectric constant and color, but also structure[9–12] when metal-ligand bond distances respond to the switched electronic state, leading to further applications as mechanical actuators.[2,13] Mechanical actuation, as well as other applications, require an interface with other materials and there are several studies of nanoscale or mesoscale heterostructures[10,14–19] combining the spin transition solids in a polymer matrix[20] or in thin films[21,22] and core-shell particles with another solid.[14–16,23–25] Experimental results, supported by theoretical predictions, reveal that at small length scales a surrounding matrix can have profound influence on the spin transition properties.[10,14,19,26–29] Generally, the as-prepared spin state, most often the high-spin (HS) state, is stabilized by the interface or matrix lowering transition temperatures. However, interfaces can also influence the mechanism and order of the phase change by altering the elastic properties of the spin transition material.[30,31]

The cobalt hexacyanoferrates, members of the cubic Prussian blue analogue (PBA) family of network solids, are among the more widely studied spin transition solids in heterostructure architectures. Cubic PBAs have the general formula $M_jA_k[B(CN)_6]_l \cdot nH_2O$ (abbreviated MAB-PBA or AB-PBA in this article) where A and B can be divalent or trivalent transition metals in ratios that depend on the relative charges of the metal ions and the number of charge-balancing cyanometallate vacancies or monovalent cations, M^+, in the structure. The cyanide bridged cobalt-iron pairs can exist as either Fe^{2+}-CN-$Co^{3+}{}_{(LS)}$ or Fe^{3+}-CN-$Co^{2+}{}_{(HS)}$ with the cobalt ion undergoing the spin-state change when changing oxidation state.[32–35] The transition between these charge states can be either thermally or optically activated, with the thermal transition from HS to LS occurring slightly below room temperature, while the light-induced transition from the LS state to a metastable HS state (photoexcited or PXHS state) is accessible below about 150 K, depending on the composition.

Nanometer scale or mesoscale (hundreds of nm to microns) particles can be readily prepared without surface modifiers[3,36] enabling fabrication of core-shel[3,14–16,23,24,30,37–41] or thin film[21,42,43] heterostructures with several isostructural PBAs. In one of the more thoroughly studied architectures, the spin-transition of a CoFe-PBA core changes the magnetization of a magnetic shell through strain-induced changes to magnetic anisotropy. Detailed structural studies have demonstrated the interplay between the spin transition material and the structurally coupled partner[15,24,29–31,40,41,44] illustrating how significant control over the elastic strain profile in spin-transition heterostructures can be exercised through deliberate design of the heterostructure geometry.

[a] J. M. Cain, W. He, D. R. Talham
Department of Chemistry, University of Florida, Gainesville, FL 32611-7200, USA
E-mail: talham@chem.ufl.edu

[b] M. W. Meisel
Department of Physics and National High Magnetic Field Laboratory, University of Florida, Gainesville, FL 32611-8440, USA
E-mail: meisel@phys.ufl.edu

Supporting information for this article is available on the WWW under https://doi.org/10.1002/ejic.202400446

Research Article
doi.org/10.1002/ejic.202400446

While studying the strain-mediated photoinduced magnetization switching in core shell particles, we observed the rate of the photoinduced spin transition establishing the photoexcited (PX) state in RbCoFe-PBA core increased by several orders of magnitude when shell was grown on the surface of the RbCoFe-PBA core, and increased further upon subsequent shell addition.[29,31] The reverse process, thermal relaxation from the PX high spin state back to the low-spin state, was also studied and a dramatic decrease in the activation energy for the relaxation process was measured upon surrounding the spin-transition core with a shell. At the same time, the presence of a shell restricts the change in core lattice constant, Δa, upon transitioning between HS and LS states and we argued[29] the lower activation energies result from reduced elastic interaction energy between transitioning sites, where, for example, a newly formed LS site acts like a defect in the surrounding HS lattice.

However, we still lack a clear understanding of the shell characteristics that influence the core elastic properties and how the core spin transition is affected by changes to its elastic properties. In the present study, we focus on this problem by comparing RbCoFe-PBA core-shell particles with different shell compositions, each across a series of shell thickness. The core-shell particles are synthesized at room temperature where the RbCoFe-PBA is in the HS state. CoCr-PBA ($a = 10.55$ Å) and KNiCr-PBA ($a = 10.45$ Å), both have larger cubic bulk lattice constants than HS RbCoFe-PBA ($a = 10.30$ Å).[15,40] In contrast, the bulk lattice parameter of KNiCo-PBA ($a = 10.10$ Å) is smaller than the HS RbCoFe-PBA.[30] As the shell modulus should change with shell type (usually scaling inversely with the lattice parameter)[26,27] and with shell thicknesses, the study allows us to interrogate the effects of shell rigidity on the core lattice as well as the influence of lattice mismatch at the core-shell interface. Our results identify the reduced misfit volume of spin transition nucleation sites, resulting from the shell-stiffened lattice of the core, as the primary contribution to the rate acceleration. However, differences in lattice mismatch between core and shell, which affect the as-synthesized strain state of the nanoparticle heterostructures, also contribute to mechanistic differences.

Results

The formulas and dimensions of the $Rb_xCo[Fe(CN)_6]_z \cdot nH_2O$ core particles and the corresponding core-shell particles used in the study are listed in Table 1. The particles were synthesized using procedures established previously,[15,29,30,39,45] based on methodology originally described by Catala *et al.*[3,46] The uniformity of the size and shape of the particles is demonstrated with TEM images, exemplified in Figure 1 for the 132 nm $Rb_{0.22}Co[Fe(CN)_6]_{0.74} \cdot nH_2O$ cores, sample 4, and the corresponding $Rb_{0.22}Co[Fe(CN)_6]_{0.74} \cdot nH_2O@(K_{0.19}Co[Cr(CN)_6]_{0.73})_{1.94} \cdot nH_2O$ core-shell sample 5, with a 19 nm shell. TEM characterization of all samples is provided in Figure S-1. The chemical formulas in Table 1 are based on ICP-AES analysis and show good consistency both within and across batches.

Figure 2 illustrates the generalized thermal and light-induced behavior as $Rb_xCo[Fe(CN)_6]_z \cdot nH_2O$ undergoes its spin transition, along with the strategy employed in this study to interrogate how the shell alters the core spin transition. The HS to LS transition was evaluated by following the thermal process, upon cooling from room temperature, as well as by following the isothermal relaxation of the metastable photoexcited HS (PXHS) back to the LS state. For the thermal process, PXRD

Table 1. Sample composition and particle dimensions.

Sample	Sample composition	Core size [a] (nm)	Shell thickness (nm)
1	$Rb_{0.36}Co[Fe(CN)_6]_{0.75} \cdot 4H_2O$	159 ± 13	0
2	$1@(K_{0.03}Co[Cr(CN)_6]_{0.7})_{0.79} \cdot 8H_2O$	159 ± 13	22
3	$1@(K_{0.01}Co[Cr(CN)_6]_{0.7})_{2.95} \cdot 16H_2O$	159 ± 13	34
4	$Rb_{0.22}Co[Fe(CN)_6]_{0.74} \cdot nH_2O$	132 ± 12	0
5	$4@(K_{0.19}Co[Cr(CN)_6]_{0.73})_{1.94} \cdot nH_2O$	132 ± 12	19
6	$Rb_{0.37}Co[Fe(CN)_6]_{0.79} \cdot nH_2O$	151 ± 14	0
7	$6@(K_{0.37}Co[Cr(CN)_6]_{0.79})_{4.25} \cdot nH_2O$	151 ± 14	47
8	$Rb_{0.28}Co[Fe(CN)_6]_{0.76} \cdot nH_2O$	147 ± 13	0
9	$8@(K_{0.28}Ni[Co(CN)_6]_{0.7})_{0.7} \cdot nH_2O$	147 ± 13	22
10	$8@(K_{0.28}Ni[Co(CN)_6]_{0.7})_{2.42} \cdot nH_2O$	147 ± 13	57
11	$Rb_{0.19}Co[Fe(CN)_6]_{0.73} \cdot 3H_2O$	122 ± 12	0
12	$11@(K_{0.19}Ni[Cr(CN)_6]_{0.73})_{0.67} \cdot 5.8H_2O$	122 ± 12	15
13	$11@(K_{0.13}Ni[Cr(CN)_6]_{0.71})_{1.78} \cdot 10H_2O$	122 ± 12	29
14	$11@(K_{0.08}Ni[Cr(CN)_6]_{0.69})_{4.49} \cdot 20H_2O$	122 ± 12	52
15	$Rb_{0.35}Co[Fe(CN)_6]_{0.77} \cdot 4H_2O$	170 ± 12	0
16	$15@(K_{0.1}Ni[Cr(CN)_6]_{0.7})_{1.44} \cdot 11H_2O$	170 ± 12	39
17	$15@(K_{0.08}Ni[Cr(CN)_6]_{0.7})_{4.01} \cdot 23H_2O$	170 ± 12	79

[a] Uncertainty in core size corresponds to standard deviation in particle distribution.

Research Article
doi.org/10.1002/ejic.202400446

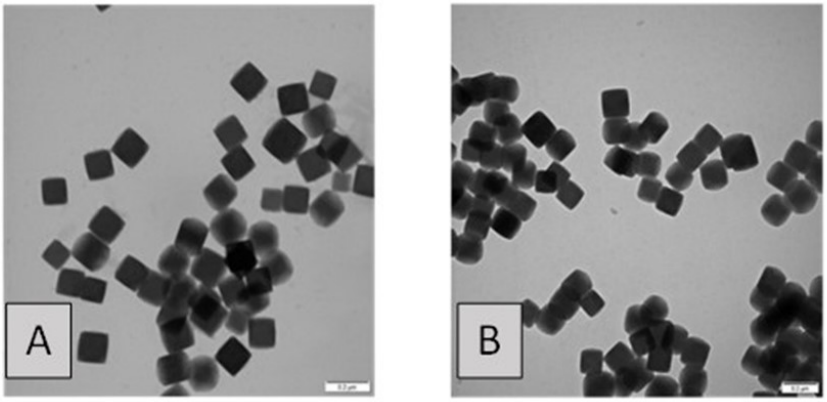

Figure 1. TEM micrographs of, (A) sample **4**, uncoated 132 nm particles of $Rb_{0.22}Co[Fe(CN)_6]_{0.74}\cdot nH_2O$ and, (B) sample **5**, core shell particles derived from sample **4** with a 19 nm shell of $(K_{0.19}Co[Cr(CN)_6]_{0.73})_{1.94}\cdot nH_2O$. Scale bars are 200 nm. Images from all samples studied are presented in Supporting Information.

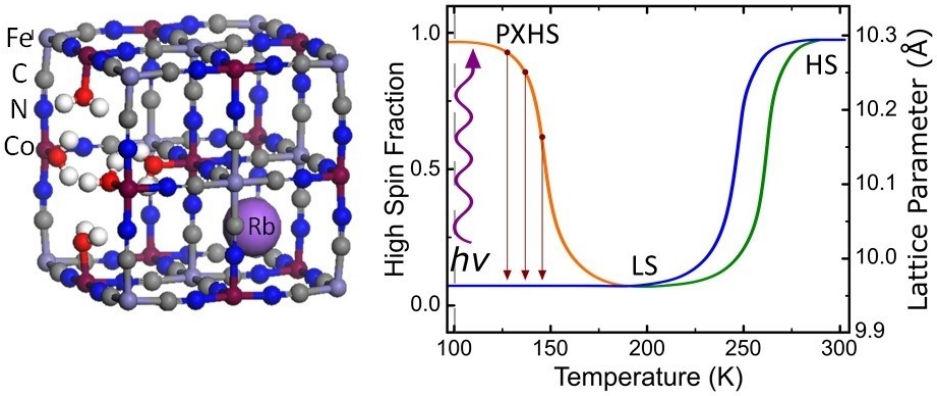

Figure 2. $Rb_xCo[Fe(CN)_6]_z\cdot nH_2O$ structure, left, and general scheme showing the thermal and light-induced spin-state switching processes, right. The blue line is the HS to LS transition upon cooling from room temperature and the green line is the reverse process, showing thermal hysteresis. Light-induced LS to HS switching at low temperature generates the PXHS state, the orange line, which thermally relaxes upon warming. The vertical lines indicate isothermal relaxation, that when conducted at different temperatures allows determination of the PXHS to LS activation energy.

patterns were collected every 2 K between room temperature and 100 K. The PXHS-to-LS relaxation was studied by first establishing the PXHS state 100 K then warming to several predetermined relaxation temperatures and monitoring the isothermal relaxation, either with PXRD or magnetometry.[29,47]

As indicated in Figure 2, there is a significant reduction in RbCoFe lattice constant when transitioning from HS to LS. As was noted in earlier studies,[29,31,40] the extent of core contraction decreases upon addition of a shell and Figure 3 plots the change in core lattice constant, $\Delta a = a_{HS} - a_{LS}$, for the bare core and for two members of each series studied here. As expected, Δa of the core decreases as shells become thicker.

Our previous study of a RbCoFe@KNiCr-PBA series correlated the extent of core contraction with the suppression of the spin transition activation energy.[29] Activation energies are most easily acquired by monitoring the isothermal relaxation of the photoexcited HS state.[29] The PXHS-to-LS relaxation was studied by first cooling samples to 100 K to establish the LS state in the RbCoFe-PBA core and then irradiating with white light for up to 3 h to achieve the PXHS state. Samples were then quickly warmed to one of several predetermined temperatures between 100–145 K, and allowed to isothermally relax back to the LS state (Figure 2). The HS fraction as a function of

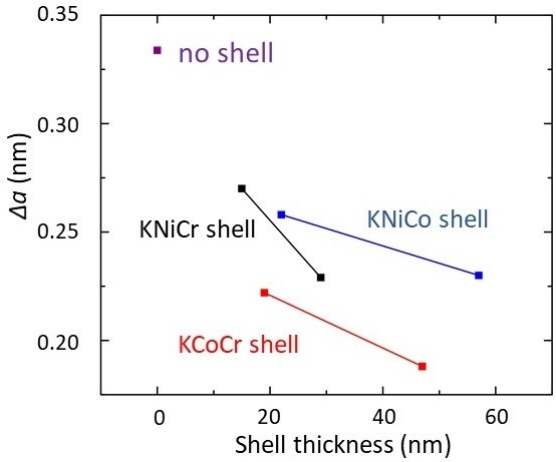

Figure 3. Changes in core lattice constant, Δa, during the spin transition of RbCoFe particles as a function of shell thickness for different shell materials. Lines connect samples with the same shell material.

Research Article
doi.org/10.1002/ejic.202400446

time was monitored using PXRD for the RbCoFe@KCoCr-PBA and RbCoFe@KNiCr-PBA series, and with magnetometry for the RbCoFe@KNiCo-PBA series as well as for the uncoated RbCoFe-PBA cores. These latter two samples were not studied with PXRD because the uncoated RbCoFe-PBA undergoes a discontinuous transition which is difficult to fit reliably, while the core and shell reflections of RbCoFe@KNiCo-PBA extensively overlap when the core is in LS state. Figure 4 provides data for RbCoFe@KCoCr-PBA with 19 nm shell, **5**, showing change in the lattice constant of both core and shell at three different temperatures. Isothermal relaxation data for the RbCoFe@KCoCr-PBA sample **7** and the RbCoFe@KNiCo-PBA samples **9** and **10** are included in Figures SI-**2**. Data for the RbCoFe@KNiCr-PBA series is taken from reference 29.

The core-shell isotherms indicate exponential decay, and the solid lines in Figures 4 and S2 are fits to an exponential decay function,

$$y = A\exp(-x/\tau) + y_0 \ , \quad (1)$$

where A is the amplitude, y_0 is the baseline, and τ is the time constant for the decay (reciprocal of the rate constant k), which monotonically decreases with increasing temperature for all samples. Arrhenius plots, Figure S3, were constructed using these time constants, and the resulting activation energies as a function of shell thickness for each series are plotted Figure 5. For each of the core-shell series, the deposition of a shell clearly has an enormous impact on the activation energy associated with the core PXHS to LS relaxation. The similarity of the activation energies across shell thicknesses for KNiCr-PBA and KNiCo-PBA shells, as well as the dissimilar response for CoCr–PBA shells, are also noteworthy, and is discussed further, below.

Seemingly contradicting our earlier observation based on a study of only the RbCoFe@KNiCr-PBA series,[29] the activation energies across the three core-shell series (Figure 5) do not simply correlate with the core Δa values (Figure 3), which were assumed to reflect the stiffness of the shell. However, the relative stiffness of the shell materials can be directly determined by monitoring both the core and shell unit cell parameters as the core contracts, which we analyzed by monitoring the thermal HS to LS transition. The thermal CTCST is particularly relevant to the study of the relaxation rate because, while it occurs at a higher temperature than the isothermal relaxation measurements, the atomic-scale mechanism is the same.[35,48] Choosing examples of similar particle size and shell thickness from each core-shell series, plots of a_{shell} vs. a_{core} are shown in Figure 6. The slopes of these plots characterize the response of the shell to a given volume reduction in the core and, therefore, reflect the relative compressibility of the shells. The slopes, β, are proportional to the shell compressi-

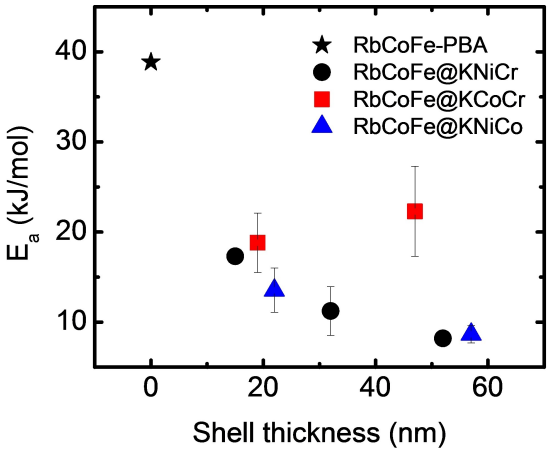

Figure 5. Activation energies from Arrhenius plots as a function of shell thickness, obtained using PXRD for RbCoFe@KCoCr-PBA and RbCoFe@KCoCr-PBA samples, and magnetometry for uncoated RbCoFe-PBA and RbCoFe@KNiCo-PBA samples.

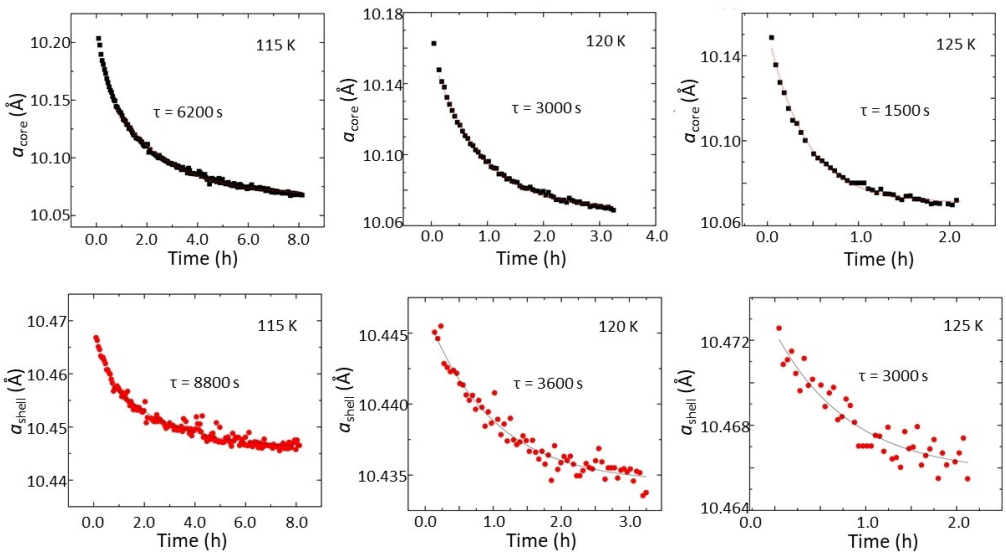

Figure 4. Plots of the normalized RbCoFe-PBA and KCoCr-PBA lattice constant during isothermal relaxation from the PXHS state for **5**, the RbCoFe@KCoCr-PBA sample with 19 nm shell. Top row: RbCoFe-PBA core. Bottom row: KCoCr-PBA shell. Fits to Equation (1) are shown using a solid line, and the resulting time constant are provided in each plot.

Research Article
doi.org/10.1002/ejic.202400446

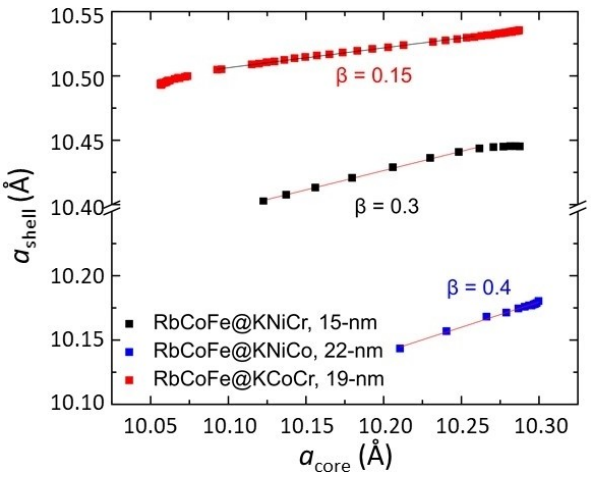

Figure 6. Lattice parameter of the shell plotted vs. the lattice parameter of the RbCoFe-PBA core while the core undergoes the thermal spin transition. The slope of the fit to the linear region, β, characterizes the response of the shell to a given volume reduction in the core.

bility and were determined from the linear portions of each plot, where a greater value of β corresponds to a softer shell. Figure 6 shows the relative stiffness of the shells is in the order KCoCr-PBA > KNiCr-PBA > KNiCo-PBA. Referring back to Figure 3, we see that the stiffest shell, KCoCr-PBA, does indeed produce the smallest values of Δa in the core, while the softest shell, KNiCo-PBA, allows the core to contract to the greatest extent.

Differential scanning calorimetry (DSC) was used to measure the thermodynamic potentials corresponding to the thermal CTCST for samples with different shell thickness from the RbCoFe@KCoCr-PBA and RbCoFe@KNiCr-PBA series and ΔH_{CTCST} and ΔS_{CTCST} are plotted vs. shell thickness in Figure 7. The magnitude of both the enthalpy and the entropy of the phase transition are suppressed in the presence of a shell to a similar extent for both series. Notably, the differences between the kinetics of the RbCoFe@KCoCr-PBA and the RbCoFe@KNiCr-PBA series in Figure 5 are not reflected in the calorimetry results, which appear very similar across the range of shell thickness.

Discussion

ΔH and Spring Constant

If the shell is responsible for the decrease in Δa of the $Rb_xCo[Fe(CN)_6]_z \cdot nH_2O$ spin transition of the core, then it is the force coming from the gradient of the elastic energy stored in the shell that keeps the core from fully contracting, and ΔH_{CTCST} for the heterostructure should be much less than for the bare cores since part of the energy from the exothermic HS-to-LS transition is used to do work on the shell instead of being released as heat. The thermodynamic data in Figure 7 showing the decrease in ΔH_{CTCST} for the core-shell samples supports this understanding.

Classically, the fact that the RbCoFe-PBA core is contracting against a "negative pressure" from the shell suggests the LS state of the core should be stiffer in the core-shell heterostructure than in the bare cores. A simplified model can be developed representing the core and shell as "springs," each one with a spring constant, w_i. In a core-shell heterostructure, the springs for core and shell will be connected in series, such that the equivalent spring constant against which the HS or PXHS state of RbCoFe-PBA must contract in order to transition to the LS state is given by

$$1/w_{eq} = 1/w_{core} + 1/w_{shell} \quad . \tag{2}$$

This relationship is illustrated in Figure 8 as a function of w_{shell}/w_{core}. Starting from large values of w_{shell}/w_{core}, the thick-shell scenario, the stiffness of the shell is equal to its bulk value. As we observed previously,[31,41] decreasing the thickness of the shell reduces the stiffness of the shell, moving along the plot to lower values of w_{shell}/w_{core}. As the shell softens, the equivalent spring constant that the spin centers in the RbCoFe-PBA must contract against in order to relax weakens. That is, the core lattice also softens. The bare-core is represented somewhere on the left-hand side of the plot, but does not go to zero, since there is always some resistance to contraction, even if only from the RbCoFe-PBA lattice itself. This very simple model also helps explain why, if the core is being stiffened, it would be less

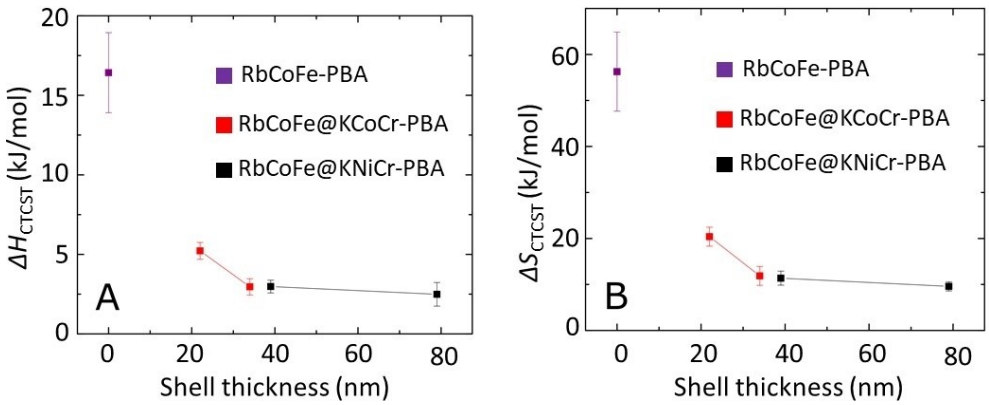

Figure 7. Phase transition thermodynamic potentials for Samples **1, 2, 3, 15** and **16**. The magnitude of both the enthalpy (A) and the entropy (B) of the phase transition are suppressed in the presence of a shell in both the RbCoFe@KCoCr-PBA series and the RbCoFe@KNiCr-PBA series.

Research Article
doi.org/10.1002/ejic.202400446

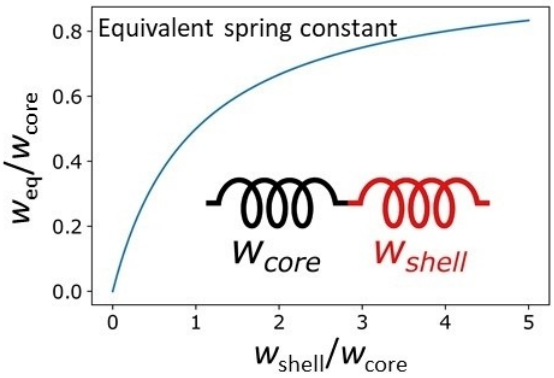

Figure 8. Scheme representing the core and shell as springs illustrating how the equivalent spring constant, w_{eq}, changes as the spring constant of the shell (w_{shell}) increases in strength (i.e., the shell becomes stiffer).

pliable with a thicker shell than with a thin shell, leading to smaller Δa for the core in the thick-shell samples. Further, the elastic energy in the spring model above is partitioned according to the following formula:

$$\frac{E_{core}}{E_{shell}} = \frac{w_{shell}}{w_{core}} \quad . \tag{3}$$

In general, the elastic energy resulting from the contraction of the core in a thin-shell sample is primarily stored in the form of strain in the shell, but for thicker shells the elastic energy is distributed more evenly between the core and shell.

Eyring Plots

While we were already able to extract the activation energies from the rate data constants using the Arrhenius plots above, transition state theory provides a framework to extract more useful information from the trends in k with temperature. In transition state theory the reactants and transition state are assumed to be in pre-equilibrium, and statistical mechanics is used to calculate the population of each state. The following derivation follows Anslyn and Dougherty.[49] The assumption of pre-equilibrium allows the rate constant for the reaction to be represented as

$$k = k'K \ , \tag{4}$$

where k' is the rate constant for the formation of products from the transition state, and K is the equilibrium constant for the pre-equilibrium. Since the formation of products from the transition state is associated with a specific vibrational mode, k' can be replaced with the frequency of the mode, ν, times a transmission coefficient (κ) describing the efficiency of product formation.

Because it is not a true equilibrium, K must also be modified to account for the lifetime of the transition state:

$$K = \left(\frac{k_B T}{h\nu}\right) K^* \ , \tag{5}$$

where k_B is Boltzmann's constant and h is Planck's constant. This new equilibrium constant K^* can be represented as $\exp(-\Delta G^{\ddagger}/RT)$, allowing Equations (4 and 5) to be recast:

$$k = \left(\frac{\kappa k_B T}{h}\right) \exp(-\Delta G^{\ddagger}/RT) \ . \tag{6}$$

As in the case with the Arrhenius equation, this equation is most useful to us in its linearized format, expanded into $\Delta H^{\ddagger}$ and $\Delta S^{\ddagger}$ terms:

$$\ln\left(\frac{kh}{\kappa k_B T}\right) = -\frac{\Delta H^{\ddagger}}{RT} + \frac{\Delta S^{\ddagger}}{R} \ . \tag{7}$$

Eyring plots were constructed for each of the samples in Figure 5, to extract the the enthalpy ($\Delta H^{\ddagger}$) and entropy ($\Delta S^{\ddagger}$) of the transition state, and the results are plotted vs. shell thickness in Figure 9. The $\Delta H^{\ddagger}$ values follow the same trend as the E_a values (Figure 5) as expected, since they can be shown to differ only by the addition of RT. However, the $\Delta S^{\ddagger}$ trend gives more information. The trend in $\Delta S^{\ddagger}$ is clearly similar to the trend in $\Delta H^{\ddagger}$, but the reason is not immediately apparent. For example, if the decrease in $\Delta H^{\ddagger}$ is due to the center of the

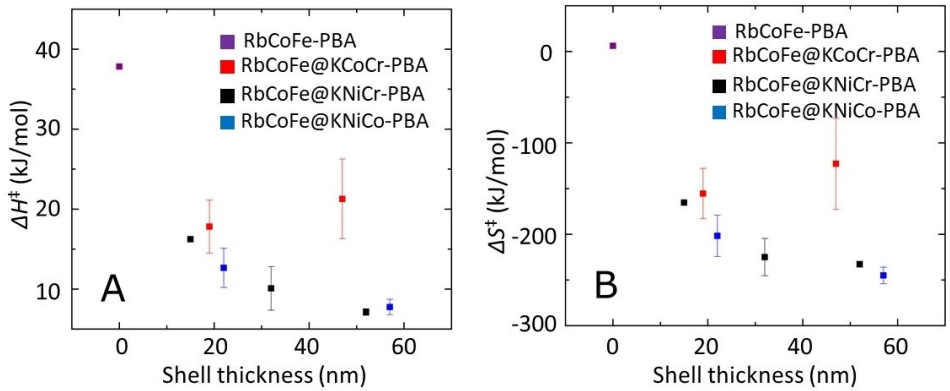

Figure 9. Transition state enthalpy (A) and entropy (B) as a function of shell thickness for samples from Figure 5.

Research Article
doi.org/10.1002/ejic.202400446

electronic wells describing the HS and LS states moving closer together along the internuclear axis, a smaller activation volume (V_A) closer to the center of the HS well would be expected. Because the relaxations are isothermal, a simple relationship results:

$$\Delta S^{\ddagger} = k_B \ln\left(\frac{V_A}{V_{HS}}\right) . \quad (8)$$

In place of $\ln\left(\frac{V_A}{V_{HS}}\right)$, we can substitute $\ln\left(\frac{a_{LS}}{a_{HS}}\right)$ from the PXRD refinements to represent the shift of the electronic wells. A plot of $\Delta S^{\ddagger}$ values from Figure 9 vs. $\ln\left(\frac{a_{LS}}{a_{HS}}\right)$ (Figure S4) shows the opposite trend from what would be expected by this argument that the differences in $\Delta S^{\ddagger}$ depend only on changes to the alignment of the electronic energy wells. On the other hand the stiffening of the core lattice with increasing shell thickness, predicted using the equivalent spring constant model, provides an alternative explanation for the decrease in $\Delta S^{\ddagger}$. If the HS center is contracting against a stiffer lattice, the number of thermally-accessible vibronic pathways to complete the transition will be decreased, leading directly to a reduction in $\Delta S^{\ddagger}$. Coupled with the calorimetry data, the transition state theory analysis provides support for a stiffened core in the core-shell particles relative to the uncoated particles.

Correlating a Stiffer Core Lattice with Lower E_{act}

To understand how the stiffened lattice lowers the HS to LS transition barrier, PXRD linewidth analysis was performed on data collected for each sample as it underwent its thermal HS to LS transition. During the early part of the transition from the HS to LS state, for example, the LS centers can be treated as defects in the lattice, with volume too small for the site they occupy.[50,51] Neglecting image effects, this defect will produce a distribution of distortions in the surrounding lattice proportional to the volume misfit, with the magnitude decreasing as the inverse square of the distance from the defect.[50] These distortions change the average distance between scatterers in PXRD, referred to as microstrain, and contribute to diffraction peak broadening.[52] Finite crystallite size also broadens PXRD peaks, and Williamson-Hall plots[53] were used in an earlier study of RbCoFe@KNiCr-PBA to deconvolute the two contributions, finding the microstrain was anisotropic, with the *hkl* reflections exhibiting much greater microstrain than the *h00* reflections.[40] A more robust method for determining the anisotropic microstrain is to incorporate it into the refinement process, especially since strain broadening tends to be Lorentzian,[54] blending very gradually into the background. A method for refining the anisotropic microstrain using the fewest parameters appropriate for the crystal system was described by Stephens and incorporated into GSAS-II.[55] For cubic systems, there are only two parameters describing the generalized microstrain, S_{400} and S_{220}. The S_{400} term is the only contribution to the microstrain of the *h00* reflections, whereas both S_{400} and S_{220} contribute to *hkl* reflections. Figure 10 shows S_{400} and S_{220} for the RbCoFe-PBA reflections in the bare cores and the first two samples in the RbCoFe@KNiCr-PBA series. As the sample is cooled from 300 K, there is a large spike in the microstrain representing the thermal CTCST of the core. This spike is clearly most pronounced in the bare cores, then is suppressed in the 15-nm shell RbCoFe@KNiCr-PBA sample and suppressed even further in the 29-nm shell RbCoFe@KNiCr-PBA sample. This suppression represents a reduction in the distribution of elastic distortions resulting from the introduction of LS defects into the HS lattice,[52] a result of the stiffened RbCoFe-PBA core lattice. In the uncoated particles, the lattice can "collapse" around the LS defect, leading to a large magnitude, long-range distortion. In the core-shell samples, however, the stiffness imparted by the shell prevents this collapse, leading to a much smaller distortion around the LS defect. The magnitude of the distortions still drops off as $\sim 1/r^2$ however, so the total distortion of the lattice during the transition is reduced in the core-shell heterostructures, which is reflected in the microstrain plots of Figure 10.

Microstrain analysis of the RbCoFe@KCoCr-PBA series is summarized in Figure 11. From the low values of Δa in the core (Figure 3), we would expect the microstrain peak should be the most suppressed in this series, as is observed. The fact that the activation energy for the RbCoFe@KCoCr-PBA series in Figure 5 changes very little with increased shell thickness is also justified

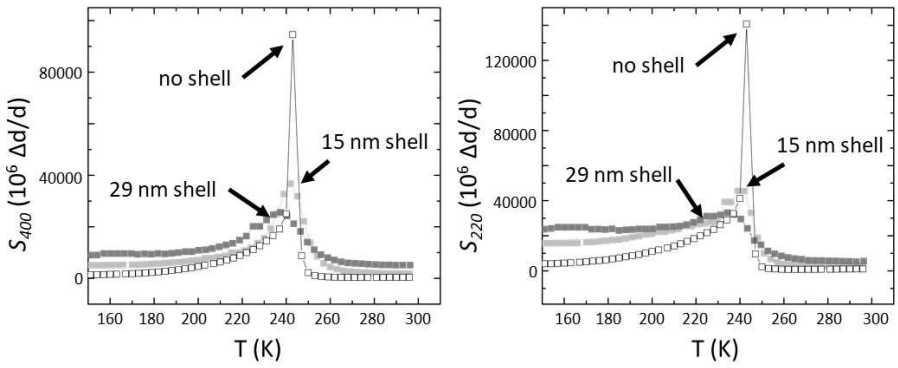

Figure 10. (A) S_{400} and (B) S_{220} for the RbCoFe-PBA reflections in the bare cores and the first two core-shell samples from the RbCoFe@KNiCr-PBA series. The spike in each plot for the uncoated cores (**Sample 11**) when undergoing the thermal CTCST is reduced in the 15-nm shell sample (**Sample 12**), and attenuated even further in the thicker shell 29-nm shell sample (**Sample 13**).

Research Article
doi.org/10.1002/ejic.202400446

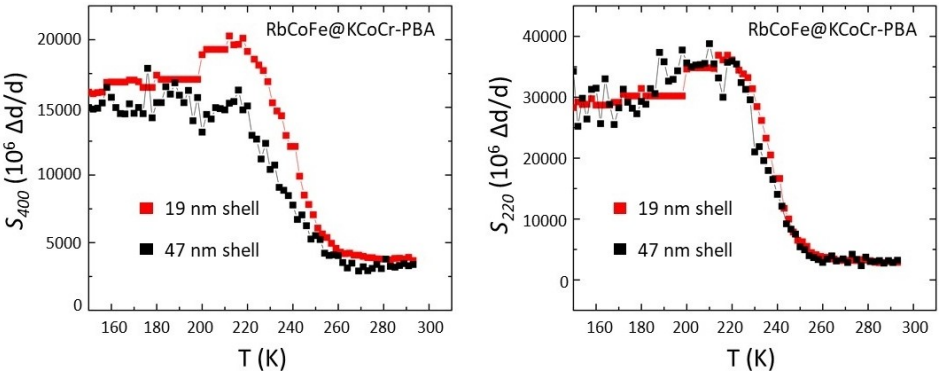

Figure 11. Left: S_{400} and Right: S_{220} for the RbCoFe-PBA reflections in the RbCoFe@KCoCr-PBA series. The spike seen in Figure 10 for the uncoated particles is barely visible in **Sample 5** (19 nm shell), and not resolvable in the thicker shell, **Sample 7** (47 nm). In contrast to Figure 10, the similarity of the plots indicates there is very little increase in core strain with the added shell volume.

by the microstrain plots, since S_{400} and S_{220} plateau at the same value for both KCoCr-PBA shell thicknesses, in contrast to the RbCoFe@KNiCr-PBA series, Figure 10, where the plateau at low temperature increases with shell thickness. The similar behavior of two shell thicknesses when measuring Δa_{core}, the magnitude of LS strain, and the PXHS to LS activation energy is consistent with previous work on RbCoFe@KCoCr-PBA particles that identified the strain depth in the KCoCr-PBA shell as 21 nm for a similar dimension core, meaning both samples are at or above the strain depth.[15]

Role of Core-Shell Lattice Misfit

Nevertheless, the defect volume misfit argument does not explain why the activation energy for the PXHS to LS relaxation is higher in the RbCoFe@KCoCr-PBA series relative to RbCoFe@-KNiCr-PBA and RbCoFe@KNiCo-PBA. Therefore, there must be another factor which influences the relaxation rate, so we next assess the influence of the core-shell lattice misfit. The microstrain plots for the *shell* reflections during the thermal CTCST are compared in Figure 12 for members of each of the three core-shell series (for the RbCoFe@KNiCo-PBA series, the analysis was limited to the temperature region where the core and shell peaks in the PXRD are well-resolved from one another). It is important to note when looking at these plots that the microstrain is normalized by the volume of shell material, which differs between each sample, so the magnitudes are not directly comparable. The most striking aspect of these plots, though, is the relaxation of the microstrain in the shell upon initial cooling for the series with negative lattice mismatch RbCoFe@KNiCo-PBA, while the two series with positive lattice mismatch, RbCoFe@KCoCr-PBA and RbCoFe@KNiCr-PBA, show an increase in microstrain upon cooling. Clearly each of the heterostructures is in a state of strain *in the as-synthesized state* due to lattice mismatch between the core and shell, and this state is expected to be present in the PX state of the RbCoFe-PBA core-shell heterostructures as well.

To show that this lattice mismatch strain has an influence on the RbCoFe-PBA core in the HS state, we return to Figures 10 and 11. There, we noted that S_{400} and S_{220} showed the same behavior with decreasing temperature. However, this similarity does not imply isotropy, because these two terms are not weighted equally in their contribution to the reflection linewidth. Figure 13 displays a series of 3D-plots showing the total microstrain at 300 K calculated from S_{400} and S_{220} for the

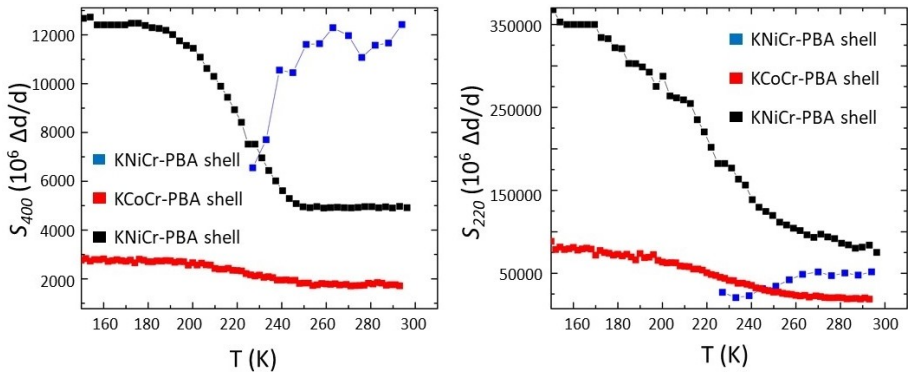

Figure 12. (A) S_{400} and (B) S_{220} for the shell reflections in Samples **7**, **9**, and **13**. The difference in magnitude reflects, in large part, the different shell volumes in each sample. While the shells with lattice parameter *a* larger than the HS RbCoFe-PBA core become more strained upon initial cooling, the strain is relieved in the KNiCo-PBA shell, which has a lattice parameter smaller than the HS RbCoFe-PBA.

Research Article
doi.org/10.1002/ejic.202400446

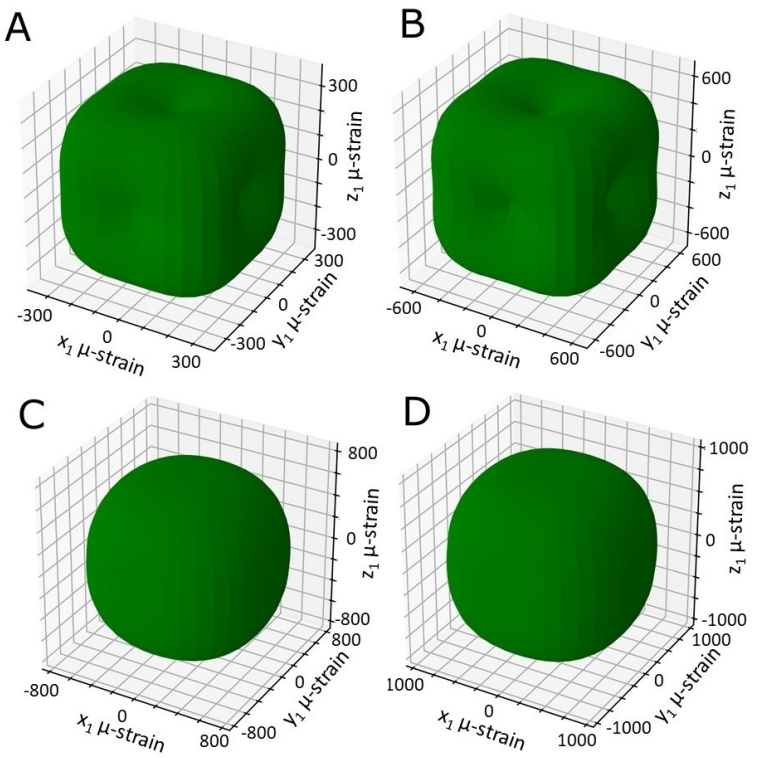

Figure 13. 3D plots showing the total microstrain in the RbCoFe-PBA core, presented as a function of reciprocal space scattering vector for (A) the as synthesized RbCoFe-PBA (**Sample 11**), and for core-shell samples (B) RbCoFe@KNiCo-PBA (**Sample 10**), (C) RbCoFe@KNiCr-PBA (**Sample 13**), and (D) RbCoFe@KCoCr-PBA (**Sample 7**). The anisotropy is accentuated in the RbCoFe@KNiCo system relative to the bare core, but the microstrain is more isotropic in the RbCoFe@KNiCr-PBA and RbCoFe@KCoCr-PBA samples. A sphere would represent isotropic strain.

RbCoFe-PBA reflections in uncoated RbCoFe-PBA, and for the core in RbCoFe@KNiCr-PBA, RbCoFe@KCoCr-PBA and RbCoFe@-KNiCo-PBA as a function of crystallographic direction. As required, these plots each show cubic symmetry. However, while the total RbCoFe-PBA microstrain in RbCoFe@KNiCr-PBA and RbCoFe@KCoCr-PBA is less anisotropic than in the uncoated RbCoFe-PBA, the total microstrain in RbCoFe@KNiCo-PBA is more anisotropic than in the bare cores. This result shows that the lattice mismatch pressure first identified in the shell microstrain plots, Figure 12, has a measureable effect on the strain state of the RbCoFe-PBA core at 300 K.

Generally the activation energy for nucleation of a LS center in a HS lattice is much smaller on a corner or near the edge of the lattice than in the center of the lattice,[56] because the surface of the lattice is able to freely contract to accommodate the defect, whereas the lattice must absorb the entirety of the elastic energy associated with the defect in the center of the lattice. With a shell deposited on the surface of the spin-transition lattice, though, we have changed the ability of the lattice edges to accommodate defect strain. Considering the conversion of a single spin center to LS in a PXHS lattice, the contraction is working 1) against the void pressure and against a small lattice mismatch pressure in the RbCoFe@KNiCr-PBA samples, 2) against the void pressure and against a large lattice mismatch pressure in the RbCoFe@KCoCr-PBA samples, and 3) against the void pressure and *with* the lattice mismatch pressure in the RbCoFe@KNiCo-PBA samples. This combination of forces explains why, despite exhibiting the smallest core Δa value of any of the series, the RbCoFe@KCoCr-PBA series has the highest activation energy barrier to relaxation.

The influence of the lattice mismatch pressure can also be seen when comparing the relaxation rates of the core lattice to that of the shell lattice in the core-shell particles. The lattice mismatch pressure is expected to have its greatest influence on the relaxation of the RbCoFe-PBA spin centers near the interface. Due to the $1/r^2$ scaling behavior of the distortion produced by a LS defect in a PXHS lattice, the lattice constant of the shell is more sensitive to the relaxation of the spin centers near the interface than those in the bulk of the core. Additionally, the change in RbCoFe-PBA lattice volume as determined via the RbCoFe-PBA PXRD reflections is more sensitive to defects in the bulk of the core than those near the interface.[36] By fitting the relaxation rates of both the core and shell, we can compare the interfacial relaxation rate to the bulk relaxation rate, and these comparisons are shown in Figure S5. For the RbCoFe@KNiCr-PBA samples, the core and shell relaxation time constants are quite similar. On the other hand, there is consistently a larger difference between the time constants for core and shell in the RbCoFe@KCoCr-PBA samples, with the shell relaxing more slowly relative to the core, indicating the HS to LS transition initiates within the core lattice, away from the interface. The situation is reversed for the RbCoFe@KNiCo-PBA sample, reacting to the lattice mismatch that favors the lower volume LS state of the core. The different

Research Article
doi.org/10.1002/ejic.202400446

behavior across the three core-shell series shows the influence of both the shell stiffness and the lattice mismatch pressure on the activation energy for the PXHS relaxation.

Comparison with Uncoated Particles

Slimani *et al.*[56] found in their MC study of the effect of long-range interactions in a relaxing spin-transition crystal that the long-range interactions between LS defects were key to getting the correct spatiotemporal evolution of the lattice, and in turn the correct relative activation energies for the relaxation. The interaction energy between two defects in a continuous medium with cubic symmetry follows Equation (9):

$$E_{int} = -\frac{15d}{8\pi\gamma^2}\Delta V^2\frac{\Gamma}{r^3}\ , \tag{9}$$

where ΔV is the volume misfit of each defect, r is the distance between them, γ is the Eshelby constant, and d and Γ are defined according to Equations (10 and 11):

$$d = c_{11} - c_{12} - 2c_{44}\ , \tag{10}$$

$$\Gamma = l^4 + m^4 + n^4 - \frac{3}{5}\ , \tag{11}$$

where c_{ij} are the elastic stiffness constants and (l,m,n) are the directional cosines of $\vec{r}$.[50] If we treat the medium as isotropic, the interaction energy between defects can be represented as $E_{int} = p_T\Delta V$, where p_T is the pressure due to one defect evaluated at the position of the other and ΔV is the volume misfit of the defect.[50] Additionally, if the effects of the surface are negligible, the interaction energy can be approximated by $E_{int} = K\Delta V^2$, where K is the bulk modulus. We can now understand why Slimani *et al.*[56] in their study of the bare cores found that the activation energy was decreased in a softened lattice due to the reduction in E_{int} resulting from a lower value for K. The value for ΔV remained relatively constant due to the ability of the free surface to accommodate the change in volume without a significant energy cost. In the presence of a shell, however, we no longer have this free surface and, as a result, the magnitude of ΔV is dramatically reduced due to the resistance from the shell. So while our system shows an increase in the stiffness with the addition of a shell, which Slimani[56] correlated with an increased activation energy barrier, we observe a suppression of the activation energy barrier because of the quadratic dependence on ΔV in Equation (9). Finally, the directional dependence of Equation (9) also helps explain observations of the reemergence of a discontinuous relaxation in **Sample 10**, where anisotropic stiffening of the lattice (Figure 13) can result in the interaction between defects becoming attractive.[1]

Conclusions

The addition of a shell to spin-transition nanoparticles dramatically alters the spin transition behavior, changing the mechanism of the solid-solid phase change from a discontinuous to a continuous transition and lowering the activation energy leading to faster kinetics. The present study attributes changes to the CTCST of RbCoFe-PBA particles to the influence of the shell on the core lattice elastic properties and correlates different shell characteristics with changes to the elastic core and the altered spin-transition. The activation energy for the relaxation of the PXHS state of RbCoFe-PBA to the LS state was found to depend on the shell thickness and the shell type in core-shell heterostructures. Evidence suggests that the LS state of the RbCoFe-PBA core is stiffened by the addition of a shell, and it is the elastic resistance from this shell that reduces the magnitude of the core's contraction during the thermal CTCST from the HS to LS state. The reduction in volume misfit for relaxing spin centers in the core-shell particles reduces the distortion of the lattice during the transition and decreases the interaction energy between LS defects in the lattice, which had earlier been shown in MC simulations to lower the activation energy for the relaxation. However, due to the lattice mismatch between the core and shell, the heterostructures are strained in the as-synthesized room-temperature state, and this lattice mismatch introduces a second, anisotropic pressure which contributes to the activation energy for relaxation through modifications to the image field, demonstrated through measurements of the relative relaxation rates of core and shell lattice reflections.

Acknowledgements

This work was supported, in part, by the Division of Materials Research (DMR) at the National Science Foundation (NSF) via DMR-1904596 (D.R.T.), DMR-1708410 (M.W.M.), and DMR-1644779 (National High Magnetic Field Laboratory). This research used the National Synchrotron Light Source II, a U.S. Department of Energy (DOE) Office of Science User Facility operated for the DOE Office of Science by Brookhaven National Laboratory under Contract No. DE-SC0012704.

Conflict of Interests

The authors declare no conflict of interest.

Data Availability Statement

The data that support the findings of this study are available in the supplementary material of this article.

Keywords: Spin crossover · core-shell · microstrain · isothermal relaxation · Prussian blue analogues

[1] I. Boldog, A. B. Gaspar, V. Martínez, P. Pardo-Ibañez, V. Ksenofontov, A. Bhattacharjee, P. Gütlich, J. A. Real, *Angew. Chem.* **2008**, *120*(34), 6533–6537.
[2] A. Enriquez-Cabrera, A. Rapakousiou, M. Piedrahita Bello, G. Molnár, L. Salmon, A. Bousseksou, *Coord. Chem. Rev.* **2020**, *419*, 213396.
[3] L. Catala, T. Mallah, *Coord. Chem. Rev.* **2017**, *346*, 32–61.
[4] A. B. Gaspar, V. Ksenofontov, M. Seredyuk, P. Gütlich, *Coord. Chem. Rev.* **2005**, *249*(23), 2661–2676.
[5] P. Gütlich, H. A. Goodwin, Spin Crossover—An Overall Perspective. *Spin Crossover in Transition Metal Compounds I*; Eds. P. Gütlich, H. A. Goodwin, ; Topics in Current Chemistry; Springer Berlin Heidelberg: Berlin, Heidelberg, **2004**; Vol. 233, 1–47..
[6] M. A. Halcrow, *Chem. Soc. Rev.* **2011**, *40*(7), 4119 .
[7] A. Bousseksou, G. Molnár, L. Salmon, W. Nicolazzi, *Chem. Soc. Rev.* **2011**, *40*(6), 3313 .
[8] E. Dobbelaar, V. B. Jakobsen, E. Trzop, M. Lee, S. Chikara, X. Ding, H. Müller-Bunz, K. Esien, S. Felton, M. A. Carpenter, E. Collet, G. G. Morgan, V. S. Zapf, *Angew. Chem. Int. Ed.* **2022**, *61*(4), e202114021.
[9] R. Torres-Cavanillas, R. Sanchis-Gual, J. Dugay, M. Coronado-Puchau, M. Giménez-Marqués, E. Coronado, *Adv. Mater.* **2019**, *31*(27), 1900039.
[10] C. R. Gros, M. K. Peprah, B. D. Hosterman, T. V. Brinzari, P. A. Quintero, M. Sendova, M. W. Meisel, D. R. Talham, *J. Am. Chem. Soc.* **2014**, *136*(28), 9846–9849.
[11] A. Galet, A. B. Gaspar, M. C. Muñoz, G. V. Bukin, G. Levchenko, J. A. Real, *Adv. Mater.* **2005**, *17*(24), 2949–2953.
[12] V. Rubio-Giménez, S. Tatay, C. Martí-Gastaldo, *Chem. Soc. Rev.* **2020**, *49*(15), 5601–5638.
[13] M. Piedrahita-Bello, J. E. Angulo-Cervera, A. Enriquez-Cabrera, G. Molnár, B. Tondu, L. Salmon, A. Bousseksou, *Mater. Horiz.* **2021**, *8*(11), 3055–3062.
[14] M. F. Dumont, E. S. Knowles, A. Guiet, D. M. Pajerowski, A. Gomez, S. W. Kycia, M. W. Meisel, D. R. Talham, *Inorg. Chem.* **2011**, *50*(10), 4295–4300.
[15] O. N. Risset, P. A. Quintero, T. V. Brinzari, M. J. Andrus, M. W. Lufaso, M. W. Meisel, D. R. Talham, *J. Am. Chem. Soc.* **2014**, *136*(44), 15660–15669.
[16] O. N. Risset, T. V. Brinzari, M. W. Meisel, D. R. Talham, *Chem. Mater.* **2015**, *27*(18), 6185–6188.
[17] A. Mosey, A. S. Dale, G. Hao, A. N'Diaye, P. A. Dowben, R. Cheng, *J. Phys. Chem. Lett.* **2020**, *11*(19), 8231–8237.
[18] M. Piedrahita-Bello, B. Martin, L. Salmon, G. Molnár, P. Demont, A. Bousseksou, *J. Mater. Chem. C* **2020**, *8*(18), 6042–6051.
[19] N. Konstantinov, A. Tauzin, U. N. Noumbé, D. Dragoe, B. Kundys, H. Majjad, A. Brosseau, M. Lenertz, A. Singh, S. Berciaud, M.-L. Boillot, B. Doudin, T. Mallah, J.-F. Dayen, *J. Mater. Chem. C* **2021**, *9*(8), 2712–2720.
[20] S. Rat, M. Piedrahita-Bello, L. Salmon, G. Molnár, P. Demont, A. Bousseksou, *Adv. Mater.* **2018**, *30*(8), 1705275.
[21] D. M. Pajerowski, M. J. Andrus, J. E. Gardner, E. S. Knowles, M. W. Meisel, D. R. Talham, *J. Am. Chem. Soc.* **2010**, *132*(12), 4058–4059.
[22] H. J. Shepherd, I. A. Gural'skiy, C. M. Quintero, S. Tricard, L. Salmon, G. Molnár, A. Bousseksou, *Nat. Commun.* **2013**, *4*(1), 2607.
[23] M. Presle, I. Maurin, F. Maroun, R. Cortès, L. Lu, R. Sayed Hassan, E. Larquet, J.-M. Guigner, E. Rivière, J. P. Wright, J.-P. Boilot, T. Gacoin, *J. Phys. Chem. C* **2014**, *118*(24), 13186–13195.
[24] A. Adam, M. Poggi, E. Larquet, R. Cortès, L. Martinelli, P.-E. Coulon, E. Lahera, O. Proux, D. Chernyshov, K. Boukheddaden, T. Gacoin, I. Maurin, *Nanoscale* **2018**, *10*(34), 16030–16039.
[25] L. Salmon, L. Catala, *Comptes. Rendus Chim.* **2018**, *21*(12), 1230–1269.
[26] A. Slimani, H. Khemakhem, K. Boukheddaden, *Phys. Rev. B* **2017**, *95*(17), 174104.
[27] H. Oubouchou, A. Slimani, K. Boukheddaden, *Phys. Rev. B* **2013**, *87*(10), 104104.
[28] K. Affes, A. Slimani, A. Maalej, K. Boukheddaden, *Chem. Phys. Lett.* **2019**, *718*, 46–53.
[29] A. C. Felts, A. Slimani, J. M. Cain, M. J. Andrus, A. R. Ahir, K. A. Abboud, M. W. Meisel, K. Boukheddaden, D. R. Talham, *J. Am. Chem. Soc.* **2018**, *140*(17), 5814–5824.
[30] W. He, J. M. Cain, M. W. Meisel, D. R. Talham, *J. Mater. Chem. C* **2021**, *9*(33), 10830–10840.
[31] J. M. Cain, W. He, I. Maurin, M. W. Meisel, D. R. Talham, *J. Appl. Phys.* **2021**, *129*(16), 160903.
[32] O. Sato, T. Iyoda, A. Fujishima, K. Hashimoto, *Science* **1996**, *272*(5262), 704–705.
[33] N. Shimamoto, S. Ohkoshi, O. Sato, K. Hashimoto, *Inorg. Chem.* **2002**, *41*(4), 678–684 .
[34] A. Bleuzen, C. Lomenech, V. Escax, F. Villain, F. Varret, C. Cartier Dit Moulin, M. Verdaguer, *J. Am. Chem. Soc.* **2000**, *122*(28), 6648–6652.
[35] C. Cartier Dit Moulin, F. Villain, A. Bleuzen, M.-A. Arrio, P. Sainctavit, C. Lomenech, V. Escax, F. Baudelet, E. Dartyge, J.-J. Gallet, M. Verdaguer, *J. Am. Chem. Soc.* **2000**, *122*(28), 6653–6658.
[36] D. Brinzei, L. Catala, N. Louvain, G. Rogez, O. Stéphan, A. Gloter, T. Mallah, *J. Mater. Chem.* **2006**, *16*(26), 2593–2599.
[37] L. Catala, F. Volatron, D. Brinzei, T. Mallah, *Inorg. Chem.* **2009**, *48*(8), 3360–3370.
[38] N. Dia, L. Lisnard, Y. Prado, A. Gloter, O. Stéphan, F. Brisset, H. Hafez, Z. Saad, C. Mathonière, L. Catala, T. Mallah, *Inorg. Chem.* **2013**, *52*(18), 10264–10274.
[39] O. N. Risset, E. S. Knowles, S. Ma, M. W. Meisel, D. R. Talham, *Chem. Mater.* **2013**, *25*(1), 42–47.
[40] A. C. Felts, M. J. Andrus, E. S. Knowles, P. A. Quintero, A. R. Ahir, O. N. Risset, C. H. Li, I. Maurin, G. J. Halder, K. A. Abboud, M. W. Meisel, D. R. Talham, *J. Phys. Chem. C* **2016**, *120*(10), 5420–5429.
[41] J. M. Cain, A. C. Felts, M. W. Meisel, D. R. Talham, *Chem. Mater.* **2021**, *33*(1), 246–255.
[42] D. M. Pajerowski, J. E. Gardner, F. A. Frye, M. J. Andrus, M. F. Dumont, E. S. Knowles, M. W. Meisel, D. R. Talham, *Chem. Mater.* **2011**, *23*(12), 3045–3053 .
[43] D. R. Talham, M. W. Meisel, *Chem. Soc. Rev.* **2011**, *40*(6), 3356.
[44] I. Maurin, M. Itoi, J. M. Cain, D. R. Talham, T. Gacoin, K. Boukheddaden, J.-P. Itié, *J. Appl. Phys.* **2021**, *129*(23), 235106.
[45] O. N. Risset, D. R. Talham, *Chem. Mater.* **2015**, *27*(11), 3838–3843.
[46] L. Catala, D. Brinzei, Y. Prado, A. Gloter, O. Stéphan, G. Rogez, T. Mallah, *Angew. Chem. Int. Ed.* **2009**, *48*(1), 183–187.
[47] C. Chong, M. Itoi, K. Boukheddaden, E. Codjovi, A. Rotaru, F. Varret, F. A. Frye, D. R. Talham, I. Maurin, D. Chernyshov, M. Castro, *Phys. Rev. B* **2011**, *84*(14), 144102.
[48] O. Sato, Y. Einaga, A. Fujishima, K. Hashimoto, *Inorg. Chem.* **1999**, *38*(20), 4405–4412.
[49] E. V. Anslyn, D. A. Dougherty, *Modern Physical Organic Chemistry*; University science: Sausalito (Calif.), **2006**.
[50] J. D. Eshelby, *Solid State Phys.* **1956**, *3*, Elsevier, 79–144.
[51] G. Félix, M. Mikolasek, G. Molnár, W. Nicolazzi, A. Bousseksou, *Eur. J. Inorg. Chem.* **2018**, *2018*(3–4), 435–442.
[52] J. G. M. Van Berkum, R. Delhez, T. De Keijser, *Acta Crystallogr. A* **1996**, *52*(5), 730–747.
[53] G. K. Williamson, W. H. Hall, *Acta Metall.* **1953**, *1*(1), 22–31.
[54] J. A. Kaduk, J. Reid, *Powder Diffr.* **2011**, *26*(1), 88–93.
[55] P. W. Stephens, *J. Appl. Crystallogr.* **1999**, *32*(2), 281–289.
[56] A. Slimani, K. Boukheddaden, K. Yamashita, *Phys. Rev. B* **2015**, *92*(1), 014111.

Manuscript received: July 16, 2024
Revised manuscript received: September 11, 2024
Accepted manuscript online: October 1, 2024
Version of record online: November 19, 2024